

# DynCFS: a program for modelling dynamic Coulomb failure stress changes in layered elastic media

Jiangcheng Zhou<sup>1,2</sup>, Rongjiang Wang<sup>3</sup> and Yong Zhang<sup>1,2</sup>

<sup>1</sup>School of Earth and Space Sciences, Peking University, Beijing 100871, China. E-mail: [zhang-yong@pku.edu.cn](mailto:zhang-yong@pku.edu.cn)

<sup>2</sup>State Key Laboratory of Earthquake Dynamics and Forecasting, Peking University, Beijing 100871, China

<sup>3</sup>GFZ Helmholtz Centre for Geosciences, Potsdam 14473, Germany

Accepted 2025 December 30. Received 2025 December 22; in original form 2025 October 29

## SUMMARY

Coulomb failure stress change ( $\Delta$ CFS) quantifies the earthquake-induced difference of shear stress and frictional resistance on a receiver fault, with the latter being proportional to the effective normal stress change.  $\Delta$ CFS has become a widely used measure for studying earthquake triggering, dynamic rupture processes and earthquake-induced secondary disasters. In simple layered or half-space elastic media, methods for computing static  $\Delta$ CFS have been well established, with programs such as Coulomb3, PSGRN-PSCMP and AutoCoulomb being widely used. In contrast, dynamic  $\Delta$ CFS evaluation generally relies on numerical discretization schemes, such as finite-difference, finite-element, boundary-element and discontinuous Galerkin methods, which, while suitable for complex structures, are computationally expensive. To overcome these limitations, we develop DynCFS, a user-friendly, Green's function based and therefore computationally efficient program for calculating both static and dynamic  $\Delta$ CFS in layered elastic media. The tool enables rapid assessment of dynamic triggering effects, both between successive earthquakes and among multiple sub-events or faults during an earthquake.

**Key words:** Numerical modelling; Computational seismology; Earthquake dynamics; Earthquake hazards; Earthquake interaction, forecasting, and prediction.

## 1 INTRODUCTION

Since the concept of Coulomb failure stress change ( $\Delta$ CFS) was introduced by G.C.P. King *et al.* (1994), it has become a fundamental physical parameter in seismology. Derived from the Coulomb failure criterion,  $\Delta$ CFS quantifies whether stress perturbations promote or inhibit fault rupture, and it has been extensively applied to studies of earthquake interaction and triggering mechanisms. Early investigations focused predominantly on static  $\Delta$ CFS, which represents the permanent stress redistribution following an earthquake and has successfully explained aftershock distributions in numerous cases (G.C.P. King *et al.* 1994; R.A. Harris 1998; R.S. Stein 1999; S. Toda *et al.* 2005). Subsequent studies increasingly highlight the importance of dynamic, that is, fully time-dependent  $\Delta$ CFS calculations for explaining dynamic triggering, noting that peak dynamic stress amplitudes can far exceed static values in the far-field where triggering can occur with peak dynamic  $\Delta$ CFS as low as 0.01 MPa (Hill *et al.* 1993; Harris 1998; J. Gomberg *et al.* 1998; Deborah Kilb *et al.* 2000; J. Gomberg *et al.* 2001; Debi Kilb *et al.* 2002; Voisin *et al.* 2004; Freed 2005; Joan Gomberg & Johnson 2005; Hill 2008; Shelly *et al.* 2011; N. Yun *et al.* 2019). Evidence also shows that transient stresses can also trigger diverse modes of fault-slip behaviours, including slow-slip events, tremors, volcanic unrest and

earthquakes at regional to teleseismic distances (Shelly *et al.* 2011; Bayramov *et al.* 2025). Meanwhile, observations of large earthquakes reveal complex, multisegment rupture processes involving cascading failures, branching and step-overs and spatiotemporally variable source mechanisms (Vallée *et al.* 2008; Y. Zhang *et al.* 2009; Schwartz *et al.* 2012; H. Zhang *et al.* 2017; Ruppert *et al.* 2018; Ulrich *et al.* 2019; Wollherr *et al.* 2019; Y. Xu *et al.* 2022; C. Ren *et al.* 2024; Stein & Bird 2024; J. Zhou *et al.* 2025). Together, these insights motivate an explicitly time-dependent view of fault interactions, for which dynamic  $\Delta$ CFS offers a natural framework to quantify wave- and rupture-front-mediated loading among faults.

Practical tools for computing static  $\Delta$ CFS in homogeneous half-space or layered elastic media have been well-established and widely adopted in routine seismological analyses. Programs such as Coulomb3 (Toda *et al.* 2011), PSCMP-PSGRN (R. Wang *et al.* 2006) and AutoCoulomb (J. Wang *et al.* 2021) are current standard resources for static stress modelling. Among these, Coulomb3 and AutoCoulomb utilize an elastic and uniform half-space model, whereas PSCMP-PSGRN is capable of calculating stress in a viscoelastic and elastic layered half-space. In contrast, dynamic  $\Delta$ CFS calculations require the computation of time-dependent stress fields from prescribed spatial-temporal rupture processes. The requisite seismic wavefields are typically obtained through sophisticated

numerical approaches, including finite-difference, finite-element, boundary-element or discontinuous-Galerkin methods. While these methods demonstrate excellent performance in fully 3-D heterogeneous media, they are computationally expensive, which limits their practical application to routine stress calculations. Alternative methods based on Green's function approaches have been developed specifically for layered half-space models. Early implementations utilizing the original Thomson–Haskell propagator algorithm (Thomson 1950; Haskell 1953; Kennett & Kerry 1979; Cotton & Coutant 1997) encountered several numerical difficulties, including precision degradation for evanescent waves (R. Wang 1999) and contamination of far-field oscillations by smooth near-field spectra (R. Wang & H. Wang 2007). These limitations were systematically addressed and resolved through a series of methodological advances by R. Wang (1999) and R. Wang et al. (2007, 2017), employing the orthonormalized propagation matrix method and differential transformations.

Building upon these theoretical and computational developments, we employ the EDGRN–EDCMP program (R. Wang 2003) to construct Green's function libraries for static stress changes, and a modified version of QSEIS (R. Wang 1999; R. Wang & H. Wang 2007) or QSSP (R. Wang et al. 2017) to compute dynamic-stress Green's functions. Integrating these robust computational components, we develop DynCFS, an open-source Python-based software tool specifically designed for computing complete  $\Delta\text{CFS}$  in layered Earth models. Our program can compute  $\Delta\text{CFS}$  on (i) receiver faults with a prescribed mechanism, (ii) receiver faults with fixed geometry but rake optimized with respect to a regional tectonic stress field and (iii) receiver faults for which both geometry and rake are optimized under a tectonic stress field. The program features streamlined installation procedures, optimized computational efficiency through vectorized operations and parallel processing capabilities, providing a convenient and rapid evaluation of both static and dynamic  $\Delta\text{CFS}$ . We apply the program to the 2008  $M_w$  7.9 Wenchuan and 2014  $M_w$  6.1 Ludian earthquakes and obtain the dynamic  $\Delta\text{CFS}$  results on a specified fault plane as well as on a plane at a fixed depth.

## 2 METHOD AND WORKFLOW

The flowchart of our program is illustrated in Fig. 1 and can be broadly divided into two parts. One part involves constructing a Green's function library of stress tensors, and the other retrieves stress tensors from the library to compute  $\Delta\text{CFS}$ .

### 2.1 Build stress tensor Green's function library

Our computational approach employs different strategies for static and dynamic stress calculations, optimized according to the spatial scale and accuracy requirements. For static stress, we construct the Green's function library using EDGRN (R. Wang 2003), a program designed to compute static stress in layered elastic half-space media. Because static  $\Delta\text{CFS}$  values are generally small in the far field, it is unnecessary to consider spherically layered Earth models. Dynamic stress calculations are performed using either QSEIS (R. Wang 1999; R. Wang & H. Wang 2007) or QSSP (R. Wang et al. 2017), depending on the epicentral distance. For near-field calculations, we employ the QSEIS program, which utilizes a layered half-space media model. Since the original QSEIS program outputs only displacement or velocity time-series, we modified the codes

to calculate stress and stress-rate tensors through analytical differentiation in the wavenumber domain (see Appendix A for details). The choice of QSEIS for near-field applications is motivated by several key advantages. In the near-field region, the Earth's spherical geometry can be well approximated by a flat layered model, enabling QSEIS to provide rapid and precise results. Furthermore, near-field stress distributions exhibit steep spatial gradients that require high spatial resolution. To achieve comparable accuracy with programs that employ spherical layered models (e.g. QSSP), extremely high harmonic degrees are necessary to satisfy the required spatial resolution, resulting in much more computational time than QSEIS. For far-field calculations where the effect of Earth's spherical geometry becomes significant, we utilized QSSP to build the stress Green's function library, which is specifically designed for computing synthetic seismograms in spherically layered media. Because Green's function calculations at different source depths are mutually independent, we parallelized the library construction and implemented two parallelization schemes to accelerate the workflow: (1) multiprocessing parallelization on a single node (personal computer) and (2) MPI-based parallelization across multiple nodes on a high-performance computing cluster. For a set of specified epicentral distances, we computed the ten non-zero stress components associated with several fundamental moment tensors (Appendix A, eqs A12.1–A12.4) to build the Green's function library, while the special case of zero epicentral distance was handled separately (Appendix A, eqs A18.1–A18.9). If a Green's function library for the same Earth model at t0h00e required numerical accuracy already exists, we proceed directly to the next stage of the calculation.

### 2.2 Compute coulomb failure stress change

We define  $\Delta\text{CFS}$  after King et al. (1994), adopting a tension-positive convention and taking the Biot coefficient to be unity ( $\alpha = 1$ ). Thus

$$\Delta\text{CFS} = \Delta\tau + \mu \cdot (\Delta\sigma_n - \Delta p), \quad (1)$$

where  $\Delta\tau$  is the shear stress change resolved in the receiver-fault slip direction,  $\Delta\sigma_n$  is the normal stress change (positive for unclamping, i.e. a decrease in compressive normal stress),  $\Delta p$  is the pore-fluid pressure change ( $p$  denotes the pore-fluid pressure; while  $p \geq 0$  in absolute terms, its perturbation  $\Delta p$  may be positive or negative), and  $\mu$  is the coefficient of friction. In a homogeneous isotropic poroelastic medium, the pore pressure change under undrained conditions is  $\Delta p = B \cdot \Delta\sigma_{kk}/3$  (Rice & Cleary 1976; Roeloffs 1996), where  $B$  is the Skempton's coefficient and  $\Delta\sigma_{kk}$  is the sum of the diagonal elements of the stress change tensor (i.e. the volumetric stress change). If we adopt the assumption that the pore pressure change is proportional to the normal stress change  $\Delta p \sim \Delta\sigma_n$ , we can employ the apparent friction coefficient (Harris 1998; Beeler et al. 2000)  $\mu' = \mu \cdot (1 - \Delta p / \Delta\sigma_n)$ . If we use the Rice model, where  $\Delta\sigma_{kk}/3$  equals  $\Delta\sigma_n$ , then we have  $\mu' = \mu \cdot (1 - B)$ . In this case, we can rewrite eq. (1) as (King et al. 1994; Harris 1998; Stein 1999; Beeler et al. 2000)

$$\Delta\text{CFS} = \Delta\tau + \mu' \cdot \Delta\sigma_n. \quad (2)$$

The established Green's function library for full stress tensor can be directly applied in calculations of eq. (1) or (2). From the Green's function library, the stress components corresponding to a specified combination of source depth, receiver depth and epicentral distance can be retrieved and combined by rotational superposition to synthesize the stress change tensor  $\Delta\sigma_e$  for a given moment tensor solution at any azimuth (Appendix A, eqs A13–A14). When

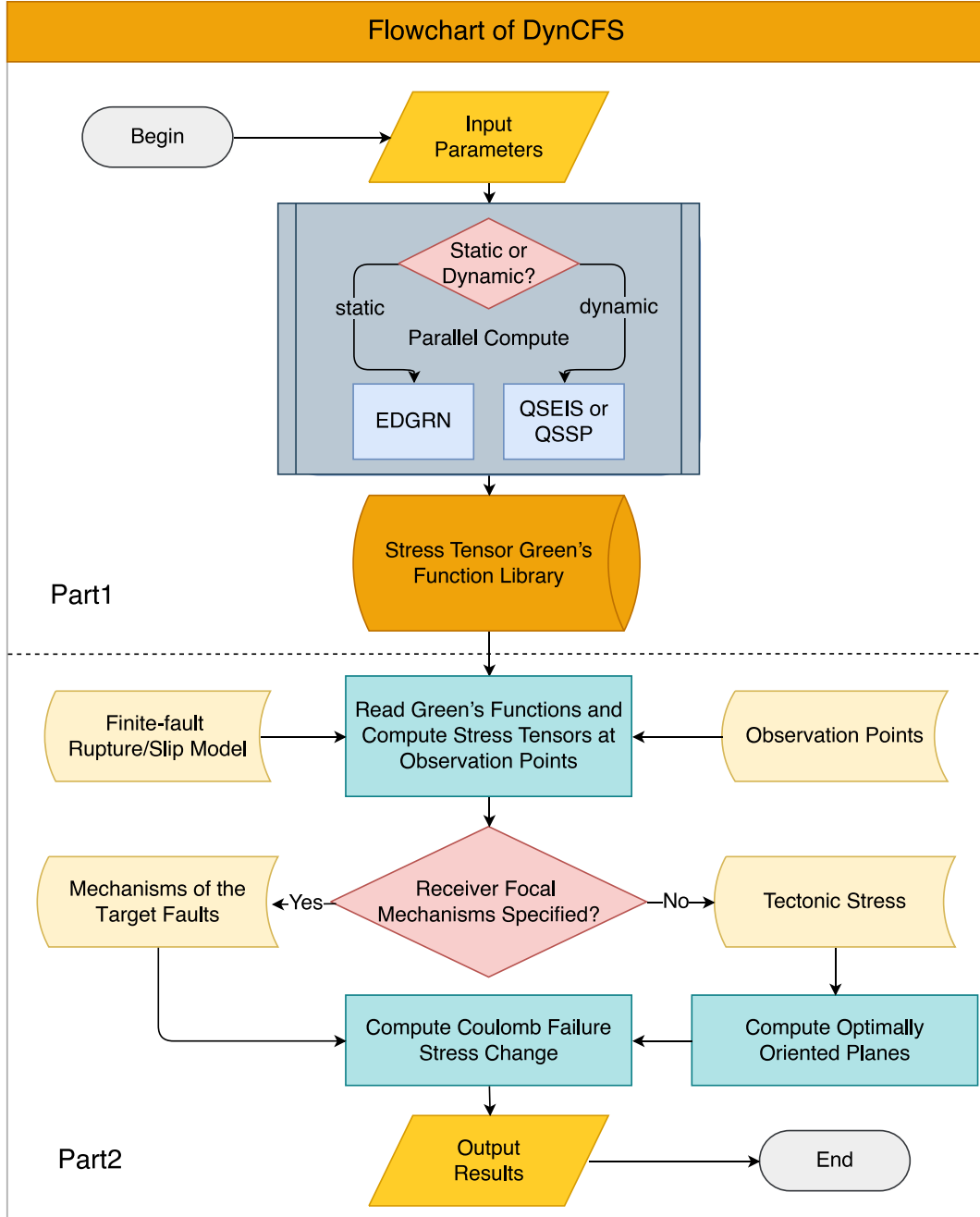


Figure 1. Flowchart of the DynCFS program.

the field point does not coincide exactly with a grid point in the Green's function library, we apply trilinear interpolation using the two nearest source depths, the two nearest receiver depths and the two nearest epicentral distances. Once the stress tensor is obtained, the traction on the receiver fault plane can be computed as

$$\Delta T_n = \Delta \sigma_e \cdot n, \quad (3)$$

where  $n$  is the unit normal vector of the receiver fault plane, and  $\Delta T_n$  is the traction change on the receiver fault plane. A subsequent vector dot product along  $n$  and the unit slip vector  $d$  yields the normal and shear stress components defined in eqs (1) and (2).

$$\Delta \sigma_n = \Delta T_n \cdot n, \quad (4.1)$$

$$\Delta \tau = \Delta T_n \cdot d. \quad (4.2)$$

The procedure described above corresponds to calculating  $\Delta CFS$  on a specified plane with fixed focal mechanism. Given a tectonic stress field, evaluating the  $\Delta CFS$  on the optimally oriented plane (OOP) is necessary. Although actual earthquakes preferentially occur on pre-existing faults, the OOP analysis remains useful as a theoretical limit or for estimating potential hazard in regions where specific fault structures have not yet been identified. The OOP is defined as the plane most susceptible to rupture according to the Mohr–Coulomb failure criterion (King *et al.* 1994), that is, the fault plane that maximizes Coulomb failure stress (CFS) after an earthquake. The definition of CFS

is

$$\text{CFS} = \tau + \mu \cdot (\sigma_n - p), \quad (5)$$

where  $\tau$  is the absolute shear stress change resolved in the receiver-fault slip direction, and  $\sigma_n$  is the absolute normal stress. For a given stress change  $\Delta\sigma_e$  induced by an earthquake, and a background tectonic stress  $\sigma_t$  at the field point, the full stress tensor is

$$\sigma = \Delta\sigma_e + \sigma_t. \quad (6)$$

The three eigenvalues  $\sigma_1$ ,  $\sigma_2$  and  $\sigma_3$  (ordered from minimum to maximum) of  $\sigma$  represent the principal stresses, and the corresponding eigenvectors  $\mathbf{n}_1$ ,  $\mathbf{n}_2$  and  $\mathbf{n}_3$  indicate the orientations of the principal stress axes. The values of  $\sigma_1$ ,  $\sigma_2$  and  $\sigma_3$  can be used to construct a 3-D Mohr's Circle representation in the  $\tau$ - $\sigma_n$  domain, as shown in Fig. 2.

Regarding the upper half of the Mohr's Circle, since any feasible stress state point inside the circle defined by  $\sigma_1$ ,  $\sigma_2$  and  $\sigma_3$  can always be shifted vertically upward to achieve a larger shear stress change  $\tau$  (and thus a larger CFS), the optimal failure point must lie on this circle (represented by the red dot in Fig. 2). And for the lower half of the Mohr's Circle, the result is symmetric. Rewriting the shear and normal stress components on this Mohr's Circle gives

$$\tau = r \sin(2\phi), \quad (7.1)$$

$$\sigma_n = r \cos(2\phi) + \sigma_0, \quad (7.2)$$

where  $r = (\sigma_3 - \sigma_1)/2$ ,  $\sigma_0 = (\sigma_3 + \sigma_1)/2$  and  $\phi$  is the angle between the normal vector of the resolved plane and  $\mathbf{n}_3$ . Combining eq. (5) with eqs (7.1) and (7.2), the Coulomb failure stress can then be written as

$$\text{CFS} = r \sqrt{\mu^2 + 1} \cos(2\phi - \gamma) + \mu (\sigma_0 - p), \quad (8)$$

with  $\gamma = \arctan(1/\mu)$ . Eq. (8) shows that the maximum CFS is attained when  $2\phi = \gamma$ . By symmetry, when  $\tau$  is reversed in sign, another plane with orientation  $2\phi = -\gamma$  yields the same maximum CFS, but with a different rupture direction. Hence, the two angles between the normal vector of OOP and  $\mathbf{n}_3$  are

$$\phi = \pm \frac{1}{2} \arctan\left(\frac{1}{\mu}\right). \quad (9)$$

Since  $p$  does not affect the value of  $\phi$ , it can be neglected when determining the OOP. It should be emphasized that  $\mu$ , rather than  $\mu'$ , should be used here, even when eq. (2) is adopted to compute  $\Delta\text{CFS}$ . This is because the statement preceding eq. (2) assumes only that  $\Delta p$  is proportional to  $\Delta\sigma_n$ , rather than  $p$  being proportional to  $\sigma_n$ , although the latter assumption has been used in some procedures such as Coulomb3. By assembling the eigenvectors  $\mathbf{n}_1$ ,  $\mathbf{n}_2$  and  $\mathbf{n}_3$  as columns to form a rotation matrix and multiplying it by the normal vector of the OOP in the principal stress coordinate system, the unit normal vector  $\mathbf{n}_{\text{OOP}}$  in the geographic coordinate system can be obtained

$$\mathbf{n}_{\text{OOP}} = [\mathbf{n}_3, \mathbf{n}_2, \mathbf{n}_1] \cdot [\cos\phi, 0, \sin\phi]^T. \quad (10)$$

And the unit slip vector  $\mathbf{d}_{\text{OOP}}$  can be calculated by

$$\mathbf{D}_{\text{OOP}} = \sigma \cdot \mathbf{n}_{\text{OOP}} - (\mathbf{n}_{\text{OOP}}^T \cdot \sigma \cdot \mathbf{n}_{\text{OOP}}) \mathbf{n}_{\text{OOP}}, \quad (11.1)$$

$$\mathbf{d}_{\text{OOP}} = \frac{\mathbf{D}_{\text{OOP}}}{|\mathbf{D}_{\text{OOP}}|}, \quad (11.2)$$

The subsequent calculation of  $\Delta\text{CFS}$  on the OOP follows the same procedure as for the specified oriented planes with fixed focal

mechanisms, described in eqs (3)–(4). It is important to note that the optimization targets CFS rather than  $\Delta\text{CFS}$ , so the unit slip vector  $\mathbf{d}_{\text{OOP}}$  is dominated by the full stress tensor  $\sigma$ . In the dynamic case, the stress at each field point varies with time, so the OOP is the most failure-prone fault plane at each time point, and consequently both the OOP normal vector and slip vector are time-dependent. If the earthquake-induced stress perturbation ( $\Delta\sigma_e$ ) is negligible relative to the tectonic stress field (i.e.  $\sigma \approx \sigma_t$ ), or when the  $\sigma_t$  inferred from geological surveys represents post-seismic conditions (i.e.  $\sigma = \sigma_t$ ), then the OOP is governed entirely by  $\sigma_t$ . Because only the OOP normal and the slip direction on the OOP are required, it suffices to know the principal stress orientations of  $\sigma_t$ ; their magnitudes are unnecessary. By contrast, when computing the optimal slip direction on a fault plane with prescribed strike and dip, one simply replaces the normal vector in eq. (11.1) with that of the plane. In this case, the full components of  $\sigma_t$ , that is, the complete stress tensor, must be provided.

### 3 VERIFICATION

We verified the key steps in  $\Delta\text{CFS}$  calculation to ensure the reliability of the DynCFS program. As a test case, we specified a source in the AK135-FC model (Kennett *et al.* 1995; Montagner & Kennett 1996), with a fault size of 1 km  $\times$  1 km, a uniform slip of 1 m, and a centroid depth at 10 km, corresponding to an  $M_W$  4.9 event. The source mechanism was set to match that of the 2008  $M_W$  7.9 Wenchuan earthquake (Y. Zhang *et al.* 2009; Y. Zhang 2010): (strike, dip, rake) = (223°, 47°, 131°). A receiver was then placed at an azimuth of 20°, an epicentral distance of 10 km and a depth of 1 km. In our calculations, we sampled the Green's function library every 0.25 s, limited the upper frequency to the Nyquist limit and used a normalized sine squared source time function (period = duration = 1.25 s) as a proxy for the  $\delta$  function. The waveforms of the stress change components at the receiver, computed with QSEIS and QSSP and low-pass filtered at 0.4 Hz, are shown in Fig. 3, and the corresponding static stress changes in the ENZ coordinate system are (in Pa):

$$\Delta\sigma_e = \begin{bmatrix} 2603 & -2029 & -545 \\ -2029 & -2557 & -1671 \\ -545 & -1671 & 185 \end{bmatrix}. \quad (12)$$

Subsequently, unless explicitly stated otherwise, all coordinate systems employ the ENZ convention with tension taken as positive. The dynamic stress components computed with QSEIS and QSSP are nearly identical, and their final values both converge to those calculated using EDGRN-EDCMP. This confirms that our procedure, building dynamic and static Green's function libraries, reading stress components and applying rotational superposition, is correct.

We next validated the calculation of static  $\Delta\text{CFS}$  for a specified receiver fault mechanism, and compared the obtained results with Coulomb3. With the slip model of the Wenchuan earthquake (Y. Zhang *et al.* 2009; Y. Zhang 2010), we computed the static  $\Delta\text{CFS}$  on receivers at 15 km depth with the same mechanism as the main event. In a homogeneous half-space, we assigned elastic properties equal to those of the AK135-FC model (Kennett *et al.* 1995; Montagner & Kennett 1996) at the source depth: Poisson's ratio 0.18 and Young's modulus  $7.3 \times 10^{10}$  Pa. We further assumed pore pressure change proportional to the normal stress change and used an apparent friction coefficient  $\mu' = 0.4$ . Figs 4(a) and (b) compare results of our program with those from Coulomb3, showing almost identical spatial patterns. The layered half-space solution is shown

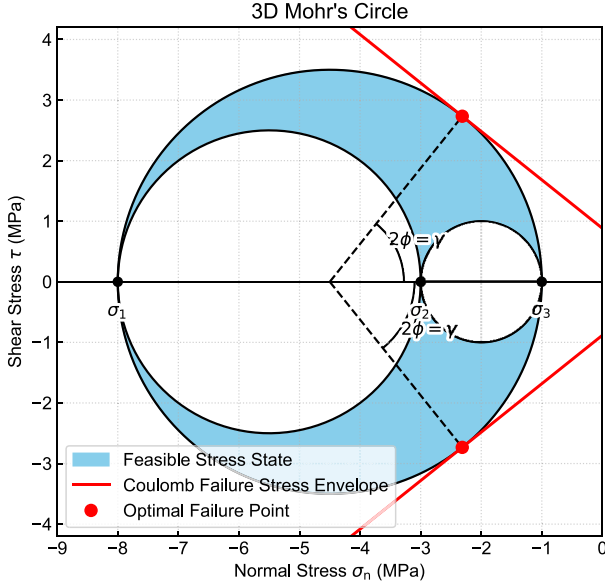


**Figure 2.** 3-D Mohr's Circle with the feasible stress state (shaded areas), Coulomb failure stress envelope (straight solid lines) and the points most susceptible to fail (tangent points).

in Fig. 4(c). To illustrate the differences between uniform half-space and layered media, we then computed the pointwise relative difference between the results shown in Figs 4(a) and (c):

$$\Delta_R = \frac{|\Delta CFS_{uni} - \Delta CFS_{lay}|}{\max(|\Delta CFS_{uni}|, |\Delta CFS_{lay}|)}, \quad (13)$$

where  $\Delta_R$  denotes the relative difference. As shown in Figs 4(a)–(c), the absolute differences between the uniform and layered media are small, whereas the  $\Delta_R$  can be significant in some regions, particularly at far-field distances where both models suggest very weak stresses. Because dynamic  $\Delta CFS$  is computed at each time step using the same procedure as the static case, the combined results of Figs 3 and 4 support the reliability of our dynamic  $\Delta CFS$  estimates on receiver planes with specified mechanism.

We then computed the static stress change using  $\mu = 0.8$  and  $B = 0.5$  for the same source and receiver as in Fig. 3 and superimposed a regional deviatoric tectonic stress on the shallow region of Longmen Shan Fault. This stress field was derived from borehole hydraulic fracturing stress data (Q. An *et al.* 2004; Y. Shi & J. Cao 2010). The minimum horizontal principal stress  $\sigma_1$  (i.e. the maximum horizontal compressive stress) is oriented N60°W with a magnitude of  $-7.5$  MPa; the maximum horizontal principal stress  $\sigma_2$  (i.e. the minimum horizontal compressive stress) is orthogonal to it with a magnitude of  $-3$  MPa; the vertical deviatoric stress  $\sigma_3$  is approximately zero. Since the lithostatic pressure does not generate shear stress and produce identical normal stress and pore pressure on any fault plane, they have no effect on OOP selection and only influence the absolute magnitude of CFS. Therefore, the tectonic stress employed here represents deviatoric stress, and the subsequent CFS values also exclude contributions from lithostatic pressures. We performed a grid search over strike, dip and rake at  $1^\circ$  increments and recorded the CFS for each combination. Fig. 5(a) displays the maximum CFS among all possible slip directions (rake angles) for each fault plane defined by specific strike and dip combinations. The fault planes corresponding to the two highest CFS values represent the OOPs. Both OOPs exhibit identical dip angles of  $26^\circ$  and rake angles of  $90^\circ$ , which is consistent with horizontal compression in the imposed tectonic stress field. The two OOPs have strikes of  $30^\circ$  and  $210^\circ$ , respectively, both perpendicular to the

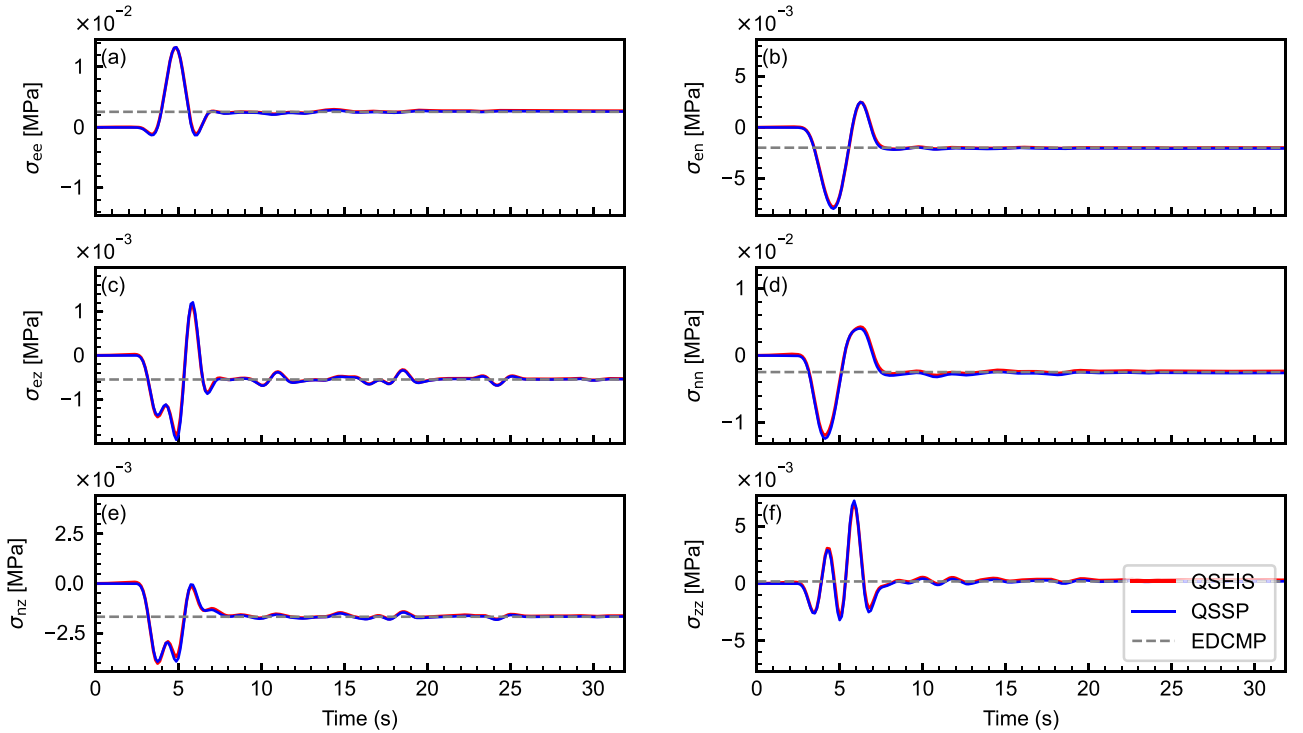


**Figure 3.** Comparison of stress components calculated by QSEIS, QSSP and EDGRN-EDCMP in the AK135-FC Earth model. The source has a mechanism of (strike, dip, rake) = (223°, 47°, 131°), a moment magnitude of  $M_W$  4.9 and a centroid depth of 10 km. The receiver is 10 km away, at an azimuth of 20° and a depth of 1 km.



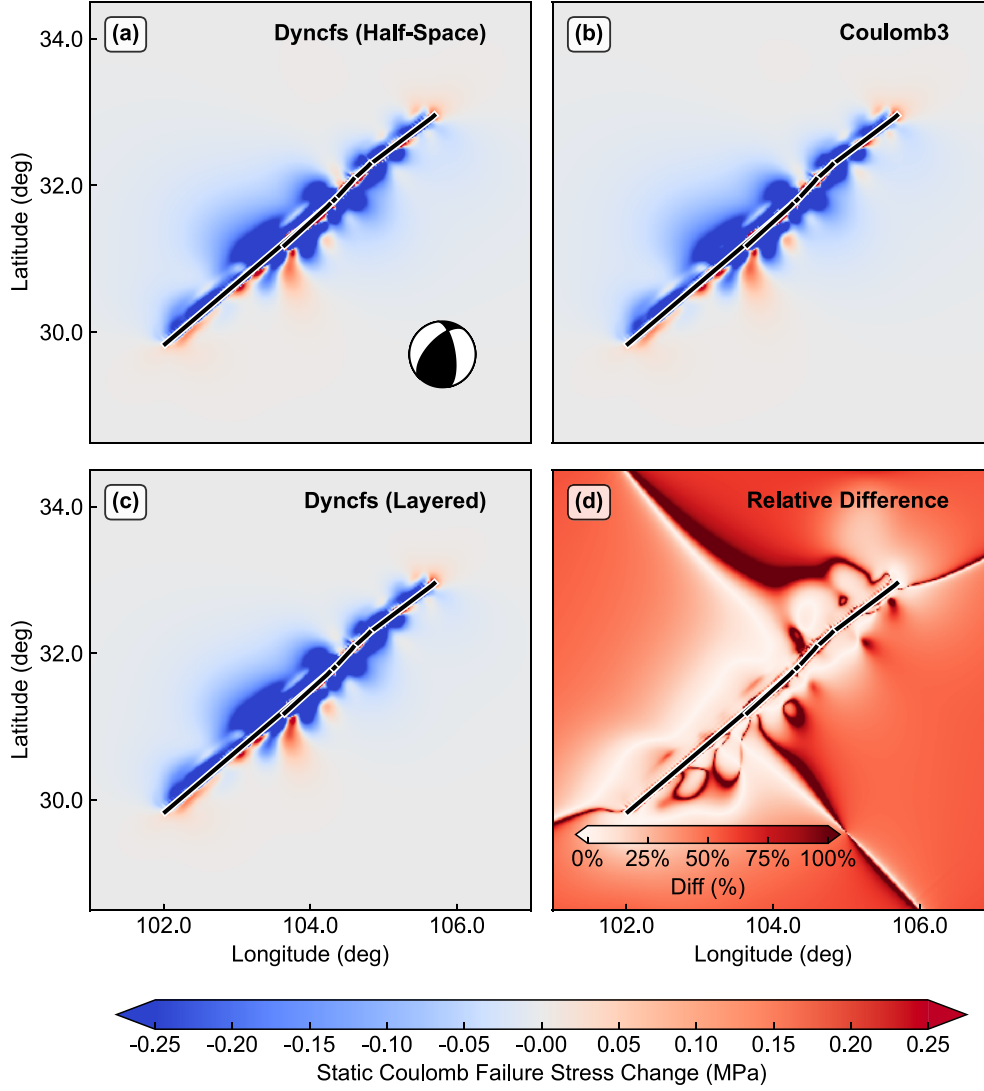


**Figure 4.** Static Coulomb failure stress change ( $\Delta\text{CFS}$ ) at 15 km depth cause by the 2008 Wenchuan earthquake. The earthquake mechanism was used as those of receiver faults. The thick black solid line marks the intersection between the main fault plane and the horizontal plane at 15 km depth. (a) Results from the DynCFS in homogeneous half-space. (b) Results from Coulomb3 in the same homogeneous half-space. (c) Results from DynCFS in layered elastic half-space. (d) Relative difference defined by eq. (13) between (a) and (c).

maximum horizontal compressive principal stress axis. The source used here, equivalent to an  $M_w$  4.9 earthquake, produces a stress change  $\Delta\sigma_e$  (eq. 12) negligible compared with the background deviatoric tectonic stress  $\Delta\sigma_t^{\text{dev}}$ . Consequently, the OOP orientation is governed almost entirely by the tectonic stress field. The two OOPs identified by the search have unit normal and slip vectors  $\mathbf{n}_1 = [-0.22, 0.38, -0.90]^T$ ,  $\mathbf{d}_1 = [0.45, -0.78, -0.44]^T$  and  $\mathbf{n}_2 = [0.22, -0.38, -0.90]^T$ ,  $\mathbf{d}_2 = [-0.45, 0.78, -0.44]^T$ , respectively, which are in agreement with the results computed analytically using eqs (9)–(11). It is worth noting that, when determining the OOP, the quantity to be maximized should be CFS rather than  $\Delta\text{CFS}$ . In Fig. 5(b), we plot the static  $\Delta\text{CFS}$  on the OOP (grey horizontal dashed line), which shows that the static  $\Delta\text{CFS}$  is small compared with the total CFS, because the total CFS is the summation of the coseismic stress perturbation and the pre-existing tectonic stress. At the same time, we also plot the dynamic  $\Delta\text{CFS}$  on the OOP at each time step in Fig. 5(b) (black curve), whose peak-to-peak amplitude is 6895 Pa, much larger in magnitude than the static value of  $-574$  Pa.

#### 4 APPLICATION: 2008 $M_w$ 7.9 WENCHUAN EARTHQUAKE

The 2008  $M_w$  7.9 Wenchuan earthquake ruptured the Longmenshan fault system at the eastern margin of the Tibetan Plateau, where NW-dipping, imbricate reverse-oblique faults accommodate convergence against the rigid Sichuan Basin (Burchfiel *et al.* 2008; Y. Zhang *et al.* 2009). Geological, geodetic and seismological studies indicate multisegment ruptures with mixed reverse and right-lateral slip on both the Yingxiu–Beichuan Fault (YBF) and the Pengguan Fault (PGF) (X. Xu *et al.* 2009; P. Zhang *et al.* 2010; Y. Li *et al.* 2010; Hartzell *et al.* 2013). The regional topography and traces of the Longmenshan system used in this study are shown in Fig. 6(a). Guided by these constraints, Y. Zhang (2010) parametrized a multiplane, mildly listric geometry including the YBF (planes S1–S4) and the PGF (plane S5) and then performed a joint finite-fault inversion that fits teleseismic, high-rate GNSS and InSAR data. The source time function and slip distribution are shown in Fig. 6(b).

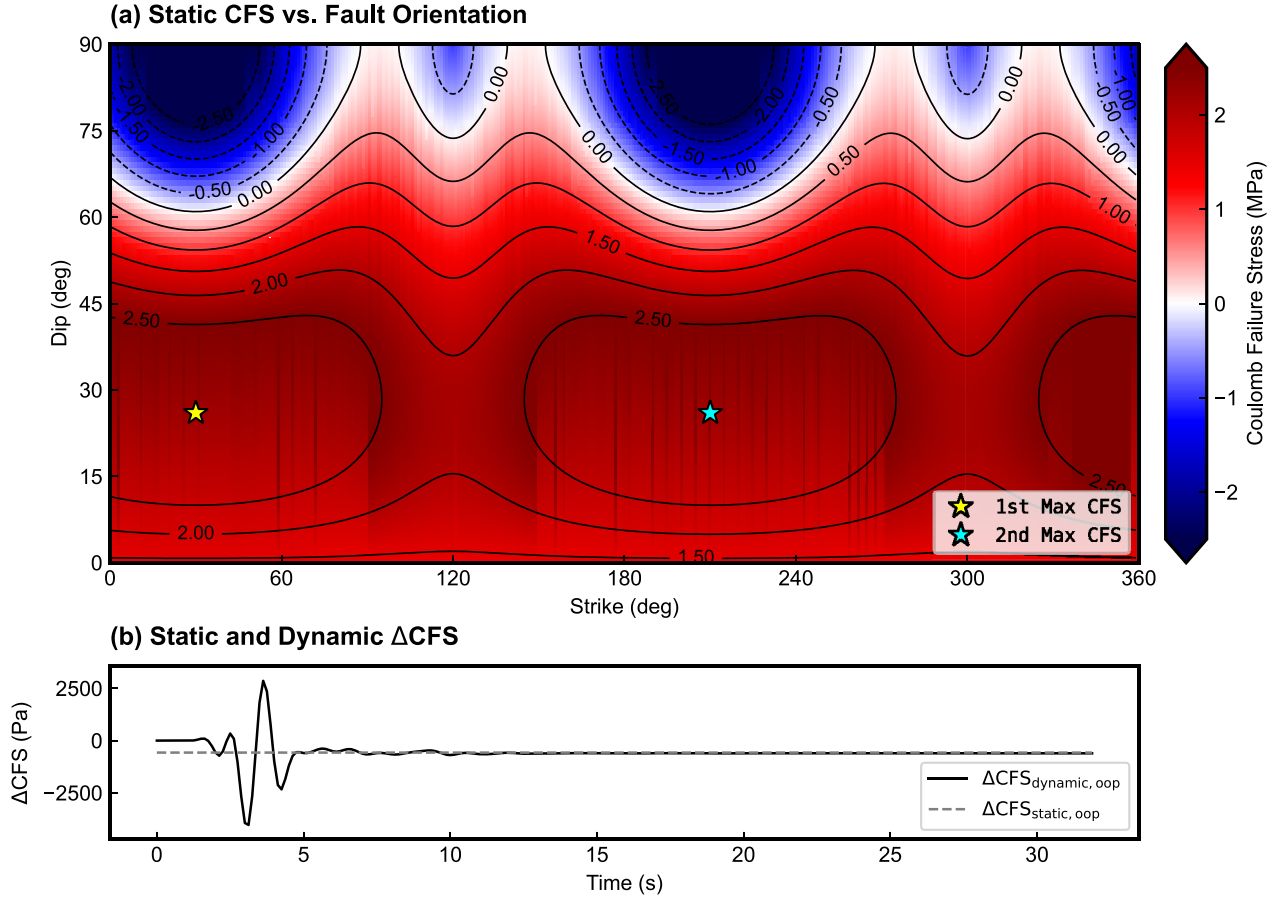


**Figure 5.** (a) Static CFS distribution relative to fault orientation. Both strike and dip are sampled at  $1^\circ$  intervals. The two stars mark the two OOPs, corresponding to CFS maxima of 3.20 MPa, with (strike, dip, rake) =  $(30^\circ, 26^\circ, 90^\circ)$  and  $(210^\circ, 26^\circ, 90^\circ)$ , respectively. (b) Static  $\Delta$ CFS on OOP (grey dashed line) and dynamic  $\Delta$ CFS evolution on time-dependent OOPs (black curve).

Using the AK135-FC Earth model, we built a Green’s function library tailored to the Wenchuan earthquake. We first constructed the static stress Green’s functions. The library spans epicentral distances out to 1000 km at a 2 km interval; source depths from 1 to 31 km at a 2 km interval and receiver depths from 0 to 32 km at a 2 km interval. Using this library and eq. (2), and assuming an effective friction coefficient  $\mu' = 0.4$ , we computed at each time the quasi-static  $\Delta$ CFS on S5 caused by the cumulative slip on S1–S4; these results are shown in the left column of Fig. 7. This can be regarded as the time evolution of  $\Delta$ CFS for a quasi-static rupture (i.e. zero rupture velocity and infinite seismic wave velocities). We then computed a dynamic stress Green’s function library with the same spatial sampling. Because the event is large and the finite-fault inversion used 5 km subfaults with an upper frequency of 0.2 Hz, we calculated dynamic stress Green’s functions using a 0.5 s time step and 1024 samples. And a normalized sine squared function (period = duration = 2.5 s) was set as a proxy for the  $\delta$  function. Based on this library and eq. (2), we computed the time-dependent dynamic  $\Delta$ CFS caused by slips on S1–S4 to the receiver fault S5, again assuming  $\mu' = 0.4$ . The resulting  $\Delta$ CFS evolution is shown in the middle column of Fig. 7, while the right column plots the slip rate history on S5. The dynamic  $\Delta$ CFS substantially exceeds the static one at nearly all time points. Approximately 18 s after rupture onset, S5 initiated rapid failure below  $\sim 15$  km depth and largely ceased by  $\sim 28$  s, accumulating a total slip of  $\sim 3.19$  m. The nucleation and subsequent growth patches of fast slip closely coincide with

regions where dynamic  $\Delta$ CFS reaches  $\sim 1$  MPa, indicating that the YBF may have dynamically triggered the PGF.

## 5 APPLICATION: 2014 $M_W$ 6.1 LUDIAN EARTHQUAKE

The 2014 August 3  $M_W$  6.1 Ludian earthquake struck the south-eastern margin of the Tibetan Plateau, near the boundary with the stable South China Block, along the conjugate Zhaotong–Ludian and Baogunao–Xiaohe faults (Y. Zhang *et al.* 2015; Y. Luo *et al.* 2018; Y. Wan *et al.* 2024). This event is widely interpreted as rupture that occurred sequentially on two conjugate fault planes (G. Zhang *et al.* 2014; Y. Wan *et al.* 2024). Guided by this view, Y. Zhang *et al.* (2015) performed a finite-fault inversion using both local and teleseismic waveform data on two conjugated planes; the resulting slip distribution is projected onto the surface in Fig. 8, together with the regional topography, focal-mechanism solution and stress field.

Because the Ludian earthquake is smaller, we adopted finer space–time sampling for the Green’s function library. We set both the static and dynamic Green’s functions to a maximum epicentral distance of 150 km sampled every 0.25 km; source depths from 0 to 20 km with a 0.5 km interval and receiver depths from 0.25 to 20.25 km with a 0.5 km spacing. Accordingly, for the dynamic Green’s functions we used a 0.125 s time step with 1024

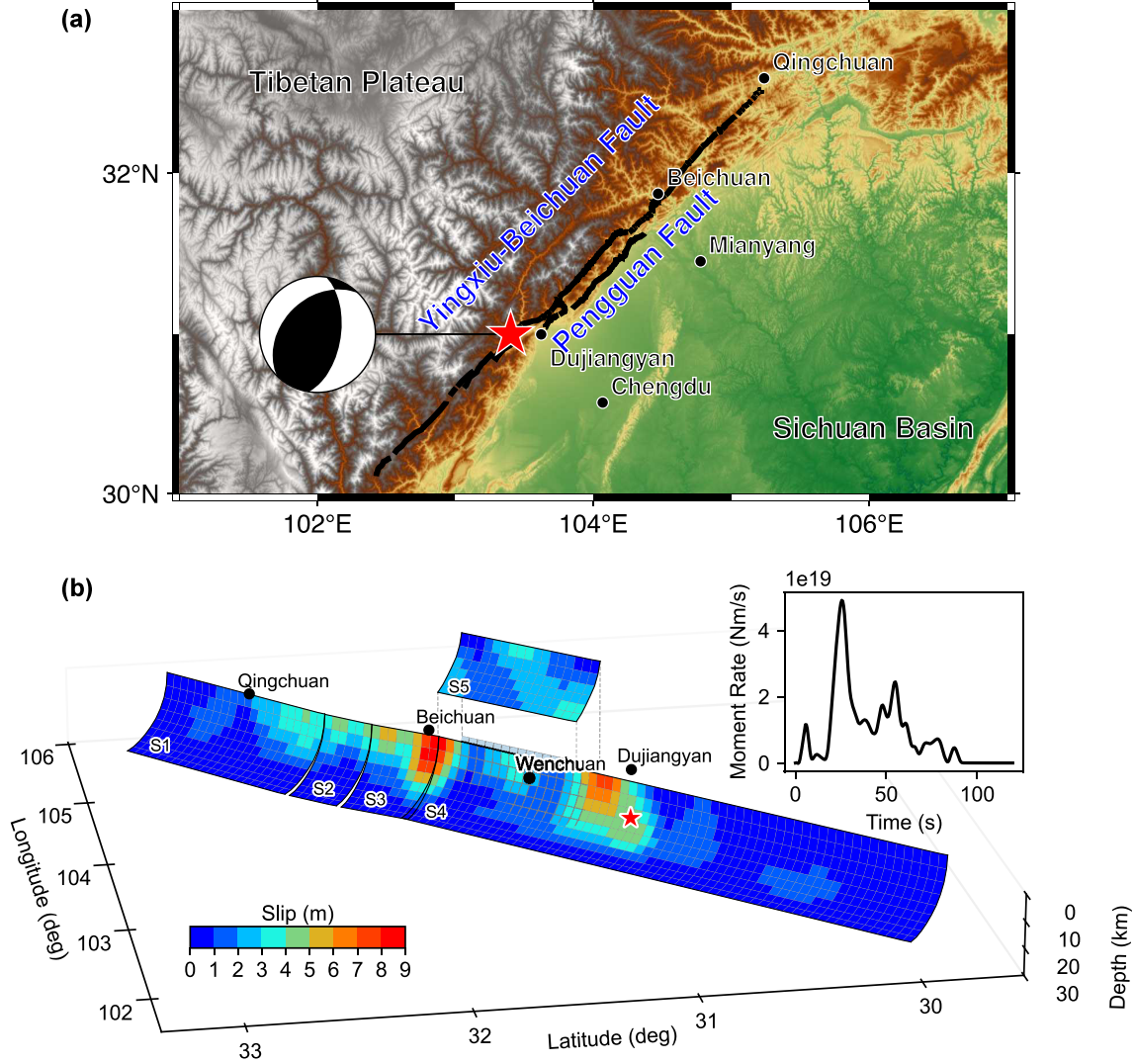


**Figure 6.** (a) Topography of the Longmenshan fault zone. The Yingxiu–Beichuan Fault (YBF) and the Pengguan Fault (PGF) are labelled, and the epicentre is marked with a star. (b) Source time function and slip distribution in the 2008  $M_W$  7.9 Wenchuan Earthquake. Fault segments S1–S4 correspond to the YBF, and S5 corresponds to the PGF (Y. Zhang 2010).

samples. We again used a normalized sine squared function (period = duration = 0.725 s) as a proxy for the  $\delta$  function. Finite-fault inversion indicates that slip was concentrated above  $\sim 5$  km on the NNW–SSE–striking fault plane, with aftershocks largely confined to depths shallower than  $\sim 10$  km. Guided by these constraints, we computed the static  $\Delta CFS$  on the OOP at 5 km depth (Fig. 9a) assuming  $\mu = 0.6$  and  $B = 0.75$ , using the regional tectonic stress field (Y. Wan *et al.* 2024). Meanwhile, we computed, at the same depth and over the same spatial domain, the dynamic stress field generated by the earthquake at each time step. Using the same regional stress field, we then determined, at each time step and for each observation point, the OOPs and the corresponding dynamic  $\Delta CFS$  resolved on those OOPs. Subsequently, we evaluated the peak-to-peak dynamic  $\Delta CFS$  over the entire sequence of time steps (defined as the maximum over all times minus the minimum over all times), as shown in Fig. 9(b). We found that near the ENE–WSW–striking fault, the aftershocks fall within the static  $\Delta CFS$  shadow (negative values) area, but correlate strongly with the peak-to-peak dynamic  $\Delta CFS$ . This pattern suggests that dynamic  $\Delta CFS$  can trigger a subset of aftershocks or, equivalently, that larger peak dynamic stresses

produce greater clock advance (J. Gombert *et al.* 1998). A similar behaviour, in which peak  $\Delta CFS$  aligns better with aftershock distribution than the static term, was documented for the 1992  $M_W$  7.3 Landers earthquake (Deborah Kilb *et al.* 2000). One interpretation is that dynamic stress perturbation effectively modifies the failure criterion and/or the characteristics and rates of rupture-promoting processes (Deborah Kilb *et al.* 2000; Debi Kilb *et al.* 2002).

## 6 DISCUSSION

Unlike the static  $\Delta CFS$  calculation, which accounts for the finite fault size or area, the dynamic  $\Delta CFS$  calculation treats each source as a point. To ensure computational accuracy, the source dimension must be reasonably small, particularly at near-field distances. In our applications to the 2008 Wenchuan and 2014 Ludian earthquakes, the subfault dimensions were neglected in the dynamic  $\Delta CFS$  computations. To evaluate the discretization error introduced by this point approximation, we first consider a  $5 \text{ km} \times 5 \text{ km}$  subfault centred at 10 km depth with focal mechanism (strike, dip, rake) =



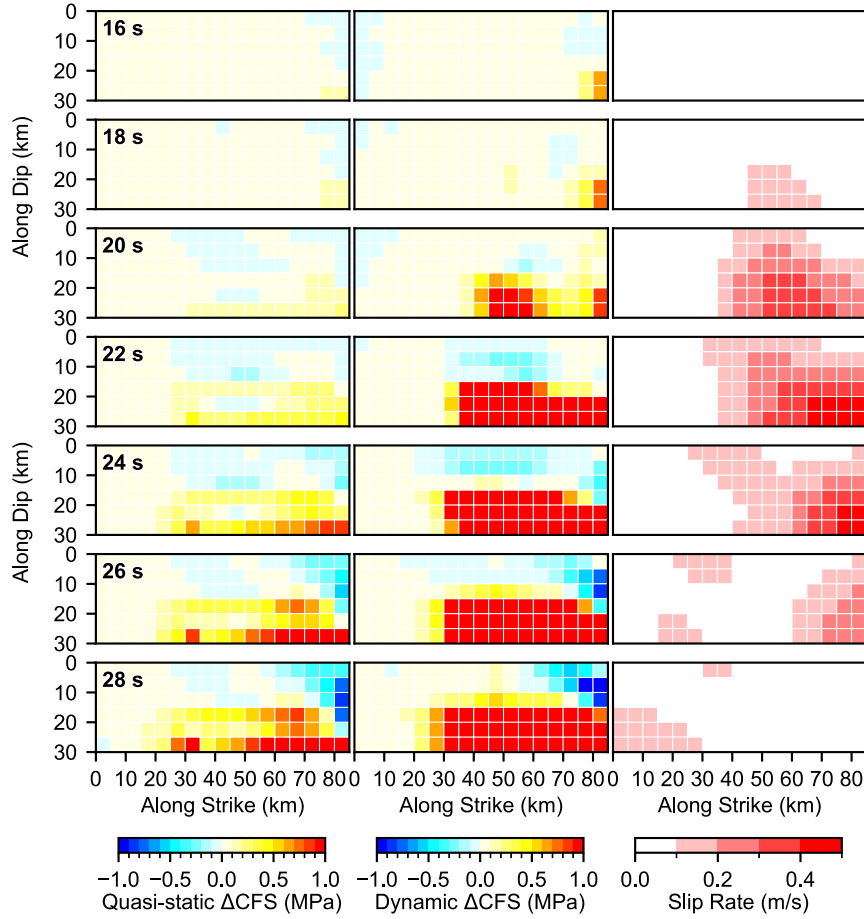


**Figure 7.** Columns from left to right show the temporal evolution of (left) quasi-static  $\Delta\text{CFS}$  on segment S5 caused by the cumulative slip on segments S1–S4, (middle) fully dynamic  $\Delta\text{CFS}$  on S5 including wave-propagation effects and (right) slip rate (Y. Zhang 2010) on S5.

( $0^\circ$ ,  $90^\circ$ ,  $0^\circ$ ). We then uniformly partition it into 4, 9, 16 and 25 smaller subfaults. For each discretization level, we compute, in a homogeneous elastic half-space, the six independent stress components at receivers located on azimuth  $45^\circ$ , at 1 km depth, for epicentral distances from 0 to 100 km. In this test we do not employ a pre-computed Green’s function library; instead, exact source–receiver stress waveforms are calculated directly, with an upper frequency of 0.2 Hz. Taking the arithmetic mean of the 25-subfault solution as the reference, the misfit is defined as the normalized RMS difference

$$\text{misfit} = \frac{\sum_i [\sigma(t_i) - \sigma_{\text{ref}}(t_i)]^2}{\sum_i [\sigma_{\text{ref}}(t_i)]^2}, \quad (14)$$

where  $\sigma(t_i)$  and  $\sigma_{\text{ref}}(t_i)$  denote the stress waveform and the reference waveform at time index  $i$ , respectively. At an epicentral distance of 15 km, the single-point approximation yields a misfit of  $\sim 0.05$  and a cross-correlation coefficient of  $\sim 0.98$  (Fig. 10), indicating that discretization errors are negligible under these conditions. In Fig. 10(c), we plot the  $\sigma_{ee}$  waveforms at an epicentral distance of 15 km for numbers of discretization points ranging from 1 to 25 as examples. The colours correspond to those in Figs 10(a) and (b). It can be seen that the waveforms for different discretization points are already very similar. The corresponding waveforms for a larger epicentral distance at 50 km are shown in Fig. 10(d), where the curves of different discretization points are almost identical. Generally, for epicentral distances exceeding about three times the

subfault dimension, discretization errors are very weak, which can be neglected.

## 7 CONCLUSION

We developed DynCFS, an open-source Python-based software tool to compute both static and dynamic Coulomb failure stress changes ( $\Delta\text{CFS}$ ) in a layered elastic half-space. The code efficiently evaluates the dynamic  $\Delta\text{CFS}$  generated by a finite-fault source on (i) receiver faults with a prescribed mechanism, (ii) receiver faults with fixed geometry but rake optimized with respect to a tectonic stress field and (iii) receiver faults for which both geometry and rake are optimized under a tectonic stress field.

DynCFS offers several advantages over existing static Coulomb stress tools and fully 3-D numerical simulations. First, it provides a unified framework to calculate both static and dynamic  $\Delta\text{CFS}$  with the same layered elastic structure, allowing direct comparison between static and dynamic triggering effects. Secondly, it employs a suite of techniques developed by R. Wang (1999) and R. Wang et al. (2007, 2017), to suppress numerical errors, which greatly reduces numerical inaccuracies compared with the conventional propagator-matrix and normal-mode summation approaches. Thirdly, by supporting both user-specified receiver planes and optimally oriented planes, the code can be used to evaluate stress changes on mapped faults as well as on potential failure planes consistent with the regional stress field. Fourthly, because it relies on 1-D layered

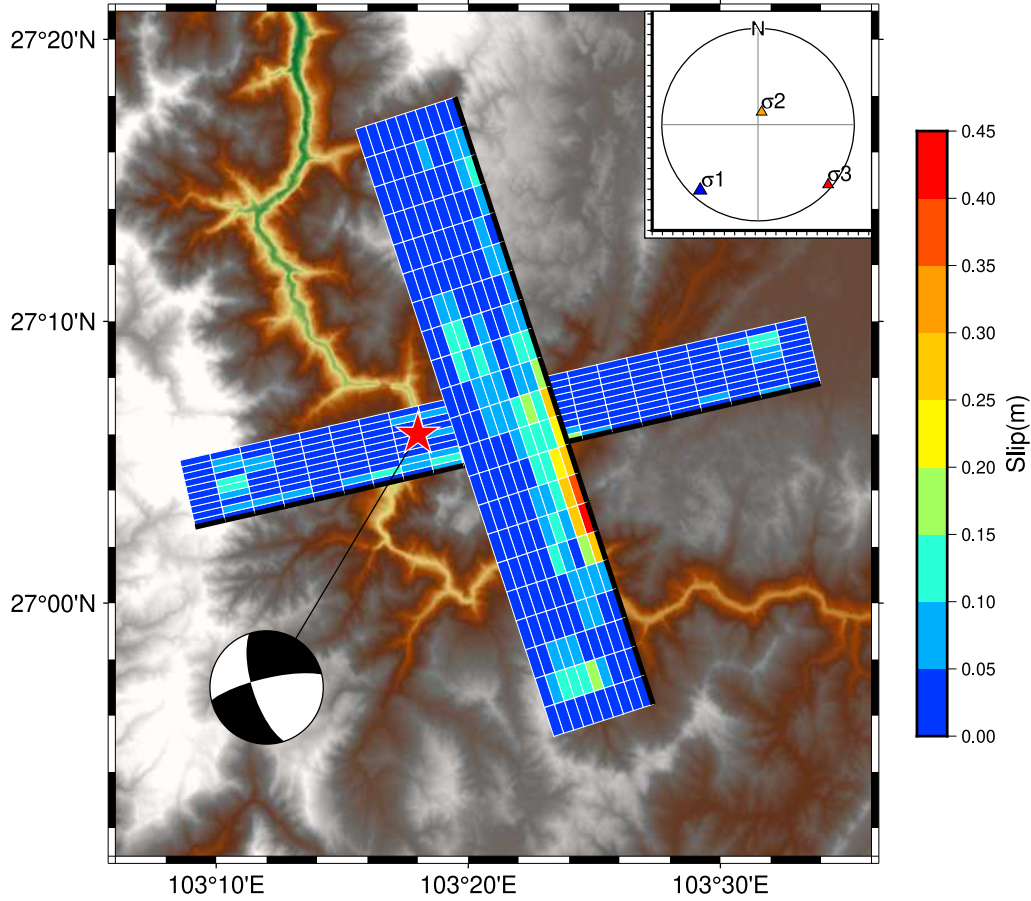


**Figure 8.** Regional topography and surface projection of slip distribution for the 2014 Ludian earthquake (Y. Zhang *et al.* 2015). The epicentre is shown by a star and the focal-mechanism (beachball) is from G. Zhang *et al.* (2014). The upper-right inset shows the lower hemisphere projection of the regional stress field (Y. Wan *et al.* 2024).

Green's functions rather than full 3-D meshes, DynCFS is computationally inexpensive and easy to apply to many source–receiver configurations, making it suitable for systematic parameter studies and routine applications. Moreover, in the near field, computing stress waveforms using normal-mode summation would require very high spherical-harmonic degrees; by instead adopting a reasonable horizontally layered-medium approximation and employing cylindrical-harmonic summation, we greatly accelerate the computation of the Green's function library. In typical applications, full simulations for a large-size finite-fault model and a dense grid of receiver points can be completed within a few hours on a mid-range 2021-era desktop processor (e.g. an AMD Ryzen 7 5800X). Finally, the implementation in Python and the open-source distribution lower the barrier to use.

We demonstrated the performance and usefulness of DynCFS with applications to the 2008  $M_w$  7.9 Wenchuan and 2014  $M_w$  6.1 Ludian earthquakes. For the Wenchuan earthquake, the calculations illuminate the spatial and temporal processes of  $\Delta$ CFS on secondary fault segments and support a dynamic triggering interpretation of the rupture of PGF (segment S5). For the Ludian earthquake, the results show that regions predicted to be static stress shadows can still experience positive dynamic  $\Delta$ CFS that correlate with the aftershock distribution, underscoring the importance of dynamic effects. These examples illustrate that DynCFS is a practical tool for studying rupture processes and stress transfer, and for quantifying dynamic triggering in layered media structures.

## ACKNOWLEDGMENTS

This work was supported by the National Key Research and Development Program of China (2022YFF0800603), and the National Natural Science Foundation of China (42021003).

## CONFLICT OF INTERESTS

The authors declare that they have no conflict of interest in relation to this study.

## DATA AVAILABILITY

The DynCFS program and two companion applications are open-sourced on GitHub: <https://github.com/Zhou-Jiangcheng/dyncfs>. A brief installation and usage guide is provided in the repository's README.md, while detailed parameter descriptions are documented in the ini files for the two applications under the example's directory.

## REFERENCES

- An, Q., Ding, L., Wang, H. & Zhao, 2004. Research of property and activity of Longmen mountain fault zone, *J. Geod. Geodyn. (in Chinese)*, **24**, 115–119.
- Bayramov, Z., Viltres, R., Doubre, C., Maggi, A., Jolivet, R. & Rivera, L., 2025. Very-long-range dynamic triggering of mud volcano unrest and silent magnitude-6 fault slip, *Science*, **389**, 996–1002.

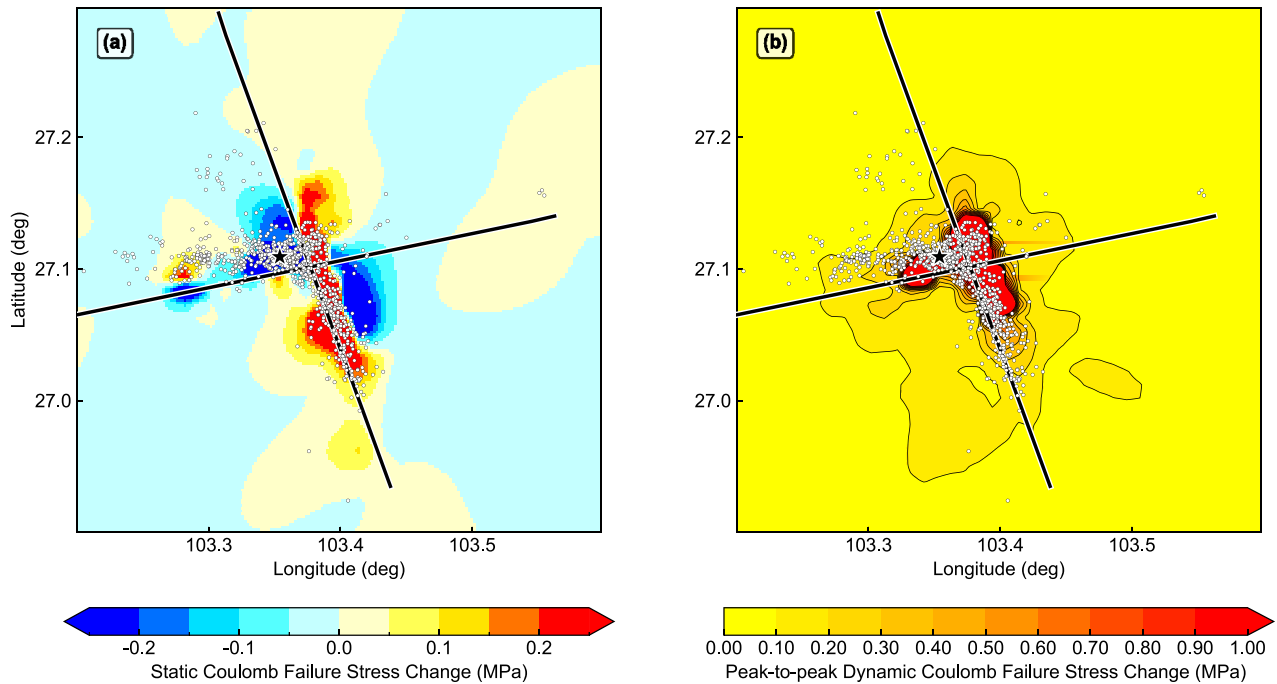


**Figure 9.** Coulomb failure stress changes on optimally oriented planes at 5 km depth and aftershocks (white circles) for the 2014  $M_W$  6.1 Ludian earthquake. Bold black lines mark the fault positions at 5 km depth. Black star denotes the epicentre. (a) Static  $\Delta CFS$ . (b) Peak-to-peak dynamic  $\Delta CFS$  resolved on the OOPs during rupture.

- Beeler, N.M., Simpson, R.W., Hickman, S.H. & Lockner, D.A., 2000. Pore fluid pressure, apparent friction, and coulomb failure, *J. geophys. Res.*, **105**, 25 533–25 542.
- Burchfiel, B.C., *et al.*, 2008. A geological and geophysical context for the Wenchuan earthquake of 12 May 2008, Sichuan, People’s Republic of China, *GSA Today*, **18**, 4.
- Cotton, F. & Coutant, O., 1997. Dynamic stress variations due to shear faults in a plane-layered medium, *Geophys. J. Int.*, **128**, 676–688.
- Freed, A.M., 2005. Earthquake triggering by static, dynamic, and postseismic stress transfer, *Annu. Rev. Earth planet. Sci.*, **33**, 335–367.
- Gomberg, J., Beeler, N.M., Blanpied, M.L. & Bodin, P., 1998. Earthquake triggering by transient and static deformations, *J. geophys. Res.: Solid Earth*, **103**, 24 411–24 426.
- Gomberg, J. & Johnson, P., 2005. Dynamic triggering of earthquakes, *Nature*, **437**, 830–830.
- Gomberg, J., Reasenberg, P.A., Bodin, P. & Harris, R.A., 2001. Earthquake triggering by seismic waves following the landers and hector mine earthquakes, *Nature*, **411**, 462–466.
- Harris, R.A., 1998. Introduction to special section: stress triggers, stress shadows, and implications for seismic hazard, *J. geophys. Res.: Solid Earth*, **103**, 24 347–24 358.
- Hartzell, S., Mendoza, C., Ramirez-Guzman, L., Zeng, Y. & Mooney, W., 2013. Rupture history of the 2008  $M_W$  7.9 Wenchuan, China, earthquake: evaluation of separate and joint inversions of geodetic, teleseismic, and strong-motion data, *Bull. seism. Soc. Am.*, **103**, 353–370.
- Haskell, N.A., 1953. The dispersion of surface waves on multilayered media, *Bull. seism. Soc. Am.*, **43**, 17–34.
- Hill, D.P., 2008. Dynamic stresses, coulomb failure, and remote triggering, *Bull. seism. Soc. Am.*, **98**, 66–92.
- Hill, D.P. *et al.*, 1993. Seismicity remotely triggered by the magnitude 7.3 landers, California, earthquake, *Science*, **260**, 1617–1623.
- Kennett, B.L.N., Engdahl, E.R. & Buland, R., 1995. Constraints on seismic velocities in the Earth from traveltimes, *Geophys. J. Int.*, **122**, 108–124.
- Kennett, B.L.N. & Kerry, N.J., 1979. Seismic waves in a stratified half space, *Geophys. J. Int.*, **57**, 557–583.
- Kilb, D., Gomberg, J. & Bodin, P., 2000. Triggering of earthquake aftershocks by dynamic stresses, *Nature*, **408**, 570–574.
- Kilb, D., Gomberg, J. & Bodin, P., 2002. Aftershock triggering by complete coulomb stress changes, *J. geophys. Res.: Solid Earth*, **107**.
- King, G.C.P., Stein, R.S. & Lin, J., 1994. Static stress changes and the triggering of earthquakes, *Bull. seism. Soc. Am.*, **84**, 935–953.
- Li, Y. *et al.*, 2010. Structural interpretation of the coseismic faults of the Wenchuan earthquake: three-dimensional modeling of the longmen shan fold-and-thrust belt, *J. geophys. Res.: Solid Earth*, **115**, 2009JB006824.
- Luo, Y., Hsieh, M. & Zhao, L., 2018. Source rupture process of the 2014 ms 6.5 Ludian, Yunnan, China, earthquake in 3D structure: the strain green’s tensor database approach, *Bull. seism. Soc. Am.*, **108**, 3270–3277.
- Montagner, J.-P. & Kennett, B.L.N., 1996. How to reconcile body-wave and normal-mode reference earth models, *Geophys. J. Int.*, **125**, 229–248.
- Ren, C., Wang, Z., Taymaz, T., Hu, N., Luo, H., Zhao, Z., Yue, H. *et al.*, 2024. Supershear triggering and cascading fault ruptures of the 2023 kahramanmaraş, türkiye, earthquake doublet, *Science*, **383**, 305–311.
- Rice, J.R. & Cleary, M.P., 1976. Some basic stress diffusion solutions for fluid-saturated elastic porous media with compressible constituents, *Rev. Geophys.*, **14**, 227–241.
- Roeloffs, E., 1996. Poroelectric techniques in the study of earthquake-related hydrologic phenomena, *Adv. Geophys.*, **37**, 135–195.
- Ruppert, N.A., Rollins, C., Zhang, A., Meng, L., Holtkamp, S.G., West, M.E. & Freymueller, J.T., 2018. Complex faulting and triggered rupture during the 2018  $M_W$  7.9 offshore kodiak, alaska, earthquake, *Geophys. Res. Lett.*, **45**, 7533–7541.
- Schwartz, D.P., Haeussler, P.J., Seitz, G.G. & Dawson, T.E., 2012. Why the 2002 denali fault rupture propagated onto the totschunda fault: implications for fault branching and seismic hazards, *J. geophys. Res.: Solid Earth*, **117**, 2011JB008918.
- Shelly, D.R., Peng, Z., Hill, D.P. & Aiken, C., 2011. Triggered creep as a possible mechanism for delayed dynamic triggering of tremor and earthquakes, *Nat. Geosci.*, **4**, 384–388.
- Shi, Y. & Cao, J., 2010. Some aspects of static stress change calculation—Case study on the wenchuan earthquake, *Chin. J. Geophys.*, **53**, 64–73.

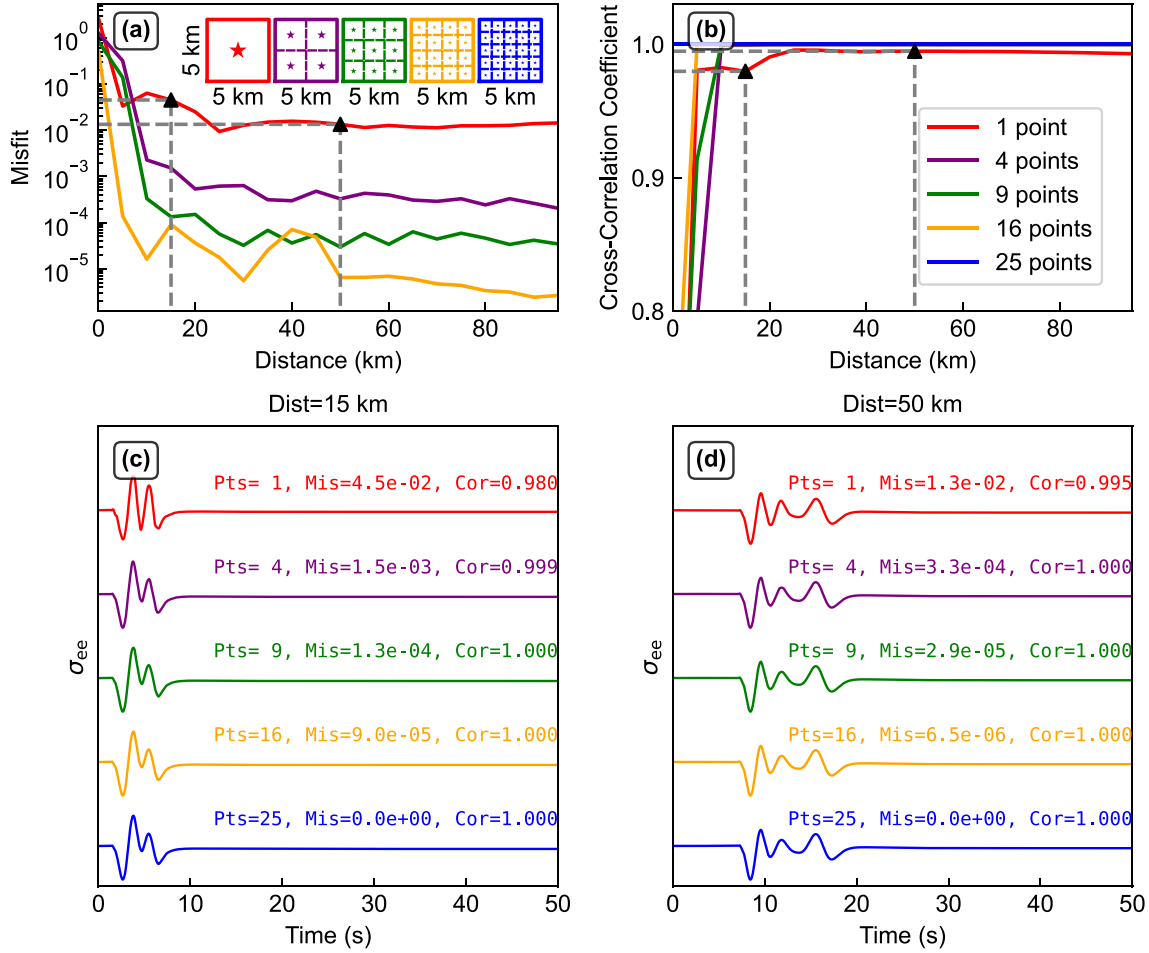


**Figure 10.** Discretization errors associated with subfault sampling. A  $5\text{ km} \times 5\text{ km}$  subfault is represented either by a single point source or by 4, 9, 16 and 25 uniformly distributed points (schematic in panel a). All points share the same focal mechanism, (strike, dip, rake) =  $(0^\circ, 90^\circ, 0^\circ)$ . The subfault centre lies at 10 km depth; the receiver is located northeast of the subfault centre (azimuth  $45^\circ$ ) at a depth of 1 km. Waveform differences are evaluated relative to the highest sampling (25 points) as epicentral distance increases. (a) Misfit versus epicentral distance. (b) Cross-correlation coefficient versus epicentral distance. (c)  $\sigma_{ee}$  stress component for different numbers of discretization points at an epicentral distance of 15 km. (d)  $\sigma_{ee}$  stress component for different numbers of discretization points at an epicentral distance of 50 km.

Stein, R.S., 1999. The role of stress transfer in earthquake occurrence, *Nature*, **402**, 605–609.

Stein, R.S. & Bird, P., 2024. Why do great continental transform earthquakes nucleate on branch faults?, *Seismol. Res. Lett.*, **95**, 3406–3415.

Thomson, W.T., 1950. Transmission of elastic waves through a stratified solid medium, *J. Appl. Phys.*, **21**, 89–93.

Toda, S., Stein, R.S., Richards-Dinger, K. & Bozkurt, S.B., 2005. Forecasting the evolution of seismicity in southern California: animations built on earthquake stress transfer, *J. geophys. Res.: Solid Earth*, **110**. doi:10.1029/2004JB003415.

Toda, S., Stein, R.S., Sevilgen, V. & Lin, J., 2011. Coulomb 3.3 graphic-rich deformation and stress-change software for earthquake, tectonic, and volcano research and teaching—User guide, *US Geol. Surv. Open-file Rep.*, **1060**, 63.

Ulrich, T., Gabriel, A.-A., Ampuero, J.-P. & Xu, W., 2019. Dynamic viability of the 2016  $M_W$  7.8 Kaikōura earthquake cascade on weak crustal faults, *Nat. Commun.*, **10**, 1213.

Vallée, M., Landès, M., Shapiro, N.M. & Klinger, Y., 2008. The 14 November 2001 Kokoxili (Tibet) earthquake: high-frequency seismic radiation originating from the transitions between sub-Rayleigh and supershear rupture velocity regimes, *J. geophys. Res.: Solid Earth*, **113**.

Voisin, C., Cotton, F. & Di Carli, S., 2004. A unified model for dynamic and static stress triggering of aftershocks, antishocks, remote seismicity,

creep events, and multisegmented rupture, *J. geophys. Res.: Solid Earth*, **109**, 2003JB002886.

Wan, Y., Song, Z., Guan, Z., Huang, R., Gu, P. & Wang, R., 2024. Discussion on reason why aftershocks of the 2014 Ludian earthquake occurred on the conjugated faults based on tectonic stress field, *Seismol. Geol. (in Chinese)*, **46**, 184–200. doi:

Wang, J., Xu, C., Freymueller, J.T., Wen, Y. & Xiao, Z., 2021. AutoCoulomb: an automated configurable program to calculate coulomb stress changes on receiver faults with any orientation and its application to the 2020  $M_W$  7.8 Simeonof Island, Alaska, earthquake, *Seismol. Res. Lett.*, **92**, 2591–2609.

Wang, R., 1999. A simple orthonormalization method for stable and efficient computation of Green's functions, *Bull. seism. Soc. Am.*, **89**, 733–741.

Wang, R., 2003. Computation of deformation induced by earthquakes in a multi-layered elastic crust—FORTRAN programs EDGRN/EDCMP, *Comput. Geosci.*, **29**, 195–207.

Wang, R., Heimann, S., Zhang, Y., Wang, H. & Dahm, T., 2017. Complete synthetic seismograms based on a spherical self-gravitating earth model with an atmosphere–ocean–mantle–core structure, *Geophys. J. Int.*, **210**, 1739–1764.

Wang, R., Lorenzo-Martin, F. & Roth, F., 2006. PSGRN/PSCMP—A new code for calculating co- and post-seismic deformation, geoid and gravity changes based on the viscoelastic-gravitational dislocation theory, *Comput. Geosci.*, **32**, 527–541 Elsevier.



- Wang, R. & Wang, H., 2007. A fast converging and anti-aliasing algorithm for green's functions in terms of spherical or cylindrical harmonics, *Geophys. J. Int.*, **170**, 239–248.
- Wollherr, S., Gabriel, A. & Mai, P.M., 2019. Landers 1992 “reloaded”: integrative dynamic earthquake rupture modeling, *J. geophys. Res.: Solid Earth*, **124**, 6666–6702.
- Xu, X., Wen, X., Yu, G., Chen, G., Klinger, Y., Hubbard, J. & Shaw, J., 2009. Coseismic reverse- and oblique-slip surface faulting generated by the 2008  $M_W$  7.9 Wenchuan earthquake, china, *Geology*, **37**, 515–518.
- Xu, Y., Zhang, Y. & Xu, L., 2022. Geometry-dependent rupture process of the 2015 Gorkha, Nepal, earthquake determined using a dip-varying inversion approach with teleseismic, high-rate GPS, static GPS and InSAR data, *Geophys. J. Int.*, **229**, 1408–1421.
- Yun, N., Zhou, S., Yang, H., Yue, H. & Zhao, L., 2019. Automated detection of dynamic earthquake triggering by the high-frequency power integral ratio, *Geophys. Res. Lett.*, **46**, 12 977–12 985.
- Zhang, G., Lei, J., Liang, S. & Sun, C., 2014. Relocations and focal mechanism solutions of the 3 August 2014 Ludian, Yunnan MS6.5 earthquake sequence, *Chin. J. Geophys. (in Chinese)*, **57**, 3018–3027.
- Zhang, H., Koper, K.D., Pankow, K. & Ge, Z., 2017. Imaging the 2016  $M_W$  7.8 Kaikoura, New Zealand, earthquake with teleseismic  $P$  waves: a cascading rupture across multiple faults: cascading rupture across multiple faults, *Geophys. Res. Lett.*, **44**, 4790–4798.
- Zhang, P.-Z., Wen, X., Shen, Z.-K. & Chen, J., 2010. Oblique, high-angle, listric-reverse faulting and associated development of strain: the Wenchuan earthquake of May 12, 2008, Sichuan, China, *Annu. Rev. Earth planet. Sci.*, **38**, 353–382.
- Zhang, Y., 2010. *Rupture Process Inversion and Its Application to the Earthquake Emergency of Large Earthquakes*, Institute of Geophysics, China Earthquake Administration.
- Zhang, Y., Chen, Y., Xu, L., Wei, X., Jin, M. & Zhang, S., 2015. The 2014  $M_W$  6.1 Ludian, Yunnan, earthquake: a complex conjugated ruptured earthquake, *Chin. J. Geophys.*, **58**, 153–162.
- Zhang, Y., Feng, W., Xu, L., Zhou, C. & Chen, Y., 2009. Spatio-temporal rupture process of the 2008 great Wenchuan earthquake, *Sci. China Ser. D-Earth Sci.*, **52**, 145–154.
- Zhou, J. *et al.*, 2025. Geometric barriers impacted rupture processes and stress releases of the 2023 kahramanmaraş, türkiye, earthquake doublet, *Commun. Earth Environ.*, **6**, 56.

## APPENDIX A. PROCEDURE FOR OBTAINING EACH STRESS COMPONENT

When solving the wave equation, we follow the orthogonal normalization propagator matrix method used in QSEIS (R. Wang 1999) and can optionally employ the differential transform to suppress numerical errors (R. Wang & H. Wang, 2007). Other formula derivations are modified from the notes of Dr Wang Rongjiang (Unpublished). Considering the spatial distribution characteristics of a horizontally layered medium, the cylindrical coordinate system is an appropriate choice. We take the upward direction as the positive  $z$ -axis, the outward direction as the positive  $r$ -axis and the counterclockwise direction as the positive  $\theta$ -axis to establish a right-handed coordinate system. When separating spatial parameters by variables, the Hankel transform is adopted. The scalar cylindrical harmonic function in the transform is defined as

$$Y_k^m(r, \theta) = J_m(kr) e^{im\theta}, \quad (\text{A1})$$

where  $k$  is the wavenumber,  $r$  is the epicentral distance,  $J_m(kr)$  is the Bessel function of the order of  $m$  and  $Y_k^m(r, \theta)$  satisfies the following equations:

$$\begin{cases} \frac{\partial^2 Y_k^m(r, \theta)}{\partial r^2} + \frac{1}{r} \frac{\partial Y_k^m(r, \theta)}{\partial r} - \frac{m^2}{r^2} Y_k^m(r, \theta) = -k^2 Y_k^m(r, \theta) \\ \frac{\partial^2 Y_k^m(r, \theta)}{\partial \theta^2} = -m^2 Y_k^m(r, \theta) \end{cases}. \quad (\text{A2})$$

Its partial derivatives with respect to  $r$  and  $\theta$  are

$$\begin{cases} \frac{\partial Y_k^m(r, \theta)}{\partial r} = k J_m'(kr) e^{im\theta} \\ \frac{\partial Y_k^m(r, \theta)}{\partial \theta} = im J_m(kr) e^{im\theta} \end{cases}. \quad (\text{A3})$$

Based on this scalar cylindrical harmonic function, the three basic functions of the vector Hankel transform can be given as

$$\begin{cases} Z_k^m(r, \theta) = e_z Y_k^m(r, \theta) \\ R_k^m(r, \theta) = (e_r \frac{\partial}{\partial r} + e_\theta \frac{\partial}{\partial \theta}) Y_k^m(r, \theta) \\ T_k^m(r, \theta) = (e_r \frac{\partial}{\partial \theta} - e_\theta \frac{\partial}{\partial r}) Y_k^m(r, \theta) \end{cases}. \quad (\text{A4})$$

If there exists a vector

$$f = U_m Z_k^m(r, \theta) + V_m R_k^m(r, \theta) + W_m T_k^m(r, \theta) = f_z e_z + f_r e_r + f_\theta e_\theta. \quad (\text{A5})$$

then its cylindrical coordinate components can be obtained from (A2)–(A5) as

$$\begin{cases} f_z = U_m J_m(kr) e^{im\theta} \\ f_r = V_m J_m'(kr) e^{im\theta} + W_m \frac{im}{kr} J_m(kr) e^{im\theta} \\ f_\theta = V_m \frac{im}{kr} J_m(kr) e^{im\theta} - W_m J_m'(kr) e^{im\theta} \end{cases}. \quad (\text{A6})$$

From the recurrence relations of the Bessel function

$$J_m'(x) = \frac{1}{2} [J_{m-1}(x) - J_{m+1}(x)], \quad (\text{A7.1})$$

$$J_m(x) = \frac{x}{2m} [J_{m-1}(x) + J_{m+1}(x)], \quad (\text{A7.2})$$

(A6) can be rewritten into a form more convenient for programming as

$$\begin{cases} f_z = U_m J_m(kr) e^{im\theta} \\ f_r = \frac{1}{2} (V_m + iW_m) J_{m-1}(kr) e^{i(m-1)\theta} - \frac{1}{2} (V_m - iW_m) J_{m+1}(kr) e^{i(m+1)\theta} \\ f_\theta = \frac{i}{2} (V_m + iW_m) J_{m-1}(kr) e^{i(m-1)\theta} + \frac{i}{2} (V_m - iW_m) J_{m+1}(kr) e^{i(m+1)\theta} \end{cases}. \quad (\text{A8})$$

When solving the wave equation in a horizontally layered medium using the propagator matrix method, the boundary conditions are continuity of displacement and continuity of stress across layers. Therefore, it is convenient to expand the displacement vector  $u(z, r, \theta)$  and the stress tensor  $\Gamma(z, r, \theta)$  by the following inverse Hankel transforms:

$$\begin{cases} u(z, r, \theta) = \sum_m \int_0^\infty (U_m Z_k^m(r, \theta) + V_m R_k^m(r, \theta) + W_m T_k^m(r, \theta)) k dk \\ e_z \cdot \Gamma(z, r, \theta) = \sum_m \int_0^\infty (E_m Z_k^m(r, \theta) + F_m R_k^m(r, \theta) + G_m T_k^m(r, \theta)) k dk \end{cases}, \quad (\text{A9})$$

so that the corresponding displacement–stress vector in the transform domain is

$$y = \begin{bmatrix} U_m \\ E_m \\ V_m \\ F_m \\ W_m \\ G_m \end{bmatrix}. \quad (\text{A10})$$

From (A8), the displacement–stress vector  $y$  can be transformed into cylindrical coordinates, yielding the three displacement components and the projection of the stress tensor in the vertical direction:

$$\begin{bmatrix} u_z \\ \sigma_{zz} \\ u_r \\ \sigma_{zr} \\ u_\theta \\ \sigma_{z\theta} \end{bmatrix} = \begin{bmatrix} U_m J_m(kr) e^{im\theta} \\ E_m J_m(kr) e^{im\theta} \\ \frac{1}{2} (V_m + iW_m) J_{m-1}(kr) e^{i(m-1)\theta} - \frac{1}{2} (V_m - iW_m) J_{m+1}(kr) e^{i(m+1)\theta} \\ \frac{1}{2} (F_m + iG_m) J_{m-1}(kr) e^{i(m-1)\theta} - \frac{1}{2} (F_m - iG_m) J_{m+1}(kr) e^{i(m+1)\theta} \\ \frac{i}{2} (V_m + iW_m) J_{m-1}(kr) e^{i(m-1)\theta} + \frac{i}{2} (V_m - iW_m) J_{m+1}(kr) e^{i(m+1)\theta} \\ \frac{i}{2} (F_m + iG_m) J_{m-1}(kr) e^{i(m-1)\theta} + \frac{i}{2} (F_m - iG_m) J_{m+1}(kr) e^{i(m+1)\theta} \end{bmatrix}. \quad (\text{A11})$$

The order of the Bessel function depends only on the radiation pattern: explosive and CLVD sources correspond to the 0th-order Bessel function, dip-slip and strike-slip sources correspond to the 1st- and 2nd-order Bessel functions, respectively. Thus, we only need to compute the following basic moment tensor components:

$$M_{\text{exp}} = \begin{bmatrix} 1 & 0 & 0 \\ 0 & 1 & 0 \\ 0 & 0 & 1 \end{bmatrix}, \quad (\text{A12.1})$$

$$M_{\text{clvd}} = \begin{bmatrix} -0.5 & 0 & 0 \\ 0 & -0.5 & 0 \\ 0 & 0 & 1 \end{bmatrix}, \quad (\text{A12.2})$$

$$M_{\text{ds1}} = \begin{bmatrix} 0 & 0 & 1 \\ 0 & 0 & 0 \\ 1 & 0 & 0 \end{bmatrix}, \quad (\text{A12.3})$$

$$M_{\text{ss1}} = \begin{bmatrix} 0 & 1 & 0 \\ 1 & 0 & 0 \\ 0 & 0 & 0 \end{bmatrix}, \quad (\text{A12.4})$$

For a fixed azimuth  $\theta_g$  (without loss of generality, let  $\theta_g=0$ ) and a range of source depths  $h_{s,g}$ , receiver depths  $h_{r,g}$  and epicentral distances  $r_g$ , the displacement–stress vector  $y_g$  serves as the Green's function library. Specifically, for explosive and CLVD sources, the tangential mode components are zero, so only the radial and vertical components need to be stored, meaning a total of 10 Green's function components. Thereafter, the physical quantities excited by any moment tensor source at any azimuth  $\theta$  can be obtained by rotation and superposition from this Green's function library. For a given combination of source depth  $h_s$ , receiver depth  $h_r$ , epicentral distance  $r$ , the corresponding quantities can be evaluated either by trilinear interpolation from neighbouring Green's functions or directly from the Green's functions at the nearest grid point. In particular, for any  $P$ – $SV$  mode physical quantity:

$$f_{P-SV}(r, \theta) = A_{\text{exp}} G_{\text{exp}}(r) + A_{\text{clvd}} G_{\text{clvd}}(r) + (A_{\text{ss1}} \sin 2\theta + A_{\text{ss2}} \cos 2\theta) G_{\text{ss}}(r) + (A_{\text{ds1}} \sin \theta + A_{\text{ds2}} \cos \theta) G_{\text{ds}}(r), \quad (\text{A13.1})$$

for any  $SH$  mode physical quantity:

$$f_{SH}(r, \theta) = (A_{\text{ss1}} \cos 2\theta - A_{\text{ss2}} \sin 2\theta) G_{\text{ss}}(r) + (A_{\text{ds1}} \sin \theta - A_{\text{ds2}} \cos \theta) G_{\text{ds}}(r), \quad (\text{A13.2})$$

where the coefficients are obtained from the given moment tensor  $M$  (in NED coordinates) as:

$$\begin{cases} A_{\text{exp}} = \frac{1}{3} (M_{11} + M_{22} + M_{33}) \\ A_{\text{clvd}} = -\frac{1}{3} (M_{11} + M_{22} - 2M_{33}) \\ A_{\text{ds1}} = M_{13}, \quad A_{\text{ds2}} = M_{23} \\ A_{\text{ss1}} = M_{12}, \quad A_{\text{ss2}} = \frac{1}{2} (M_{11} - M_{22}) \end{cases}. \quad (\text{A14})$$

The above describes the construction of the Green's function library for displacement and stress projected in the  $z$ -direction, and the theoretical method for synthetic seismograms. In cylindrical coordinates, the strain components are:

$$\begin{cases} \varepsilon_{zz} = \frac{\partial u_z}{\partial z} \\ \varepsilon_{rr} = \frac{\partial u_r}{\partial r} \\ \varepsilon_{\theta\theta} = \frac{1}{r} \left( u_r + \frac{\partial u_\theta}{\partial \theta} \right) \\ \varepsilon_{zr} = \frac{1}{2} \left( \frac{\partial u_z}{\partial r} + \frac{\partial u_r}{\partial z} \right) \\ \varepsilon_{z\theta} = \frac{1}{2} \left( \frac{1}{r} \frac{\partial u_z}{\partial \theta} + \frac{\partial u_\theta}{\partial z} \right) \\ \varepsilon_{r\theta} = \frac{1}{2} \left( \frac{1}{r} \frac{\partial u_r}{\partial \theta} + \frac{\partial u_\theta}{\partial r} - \frac{u_\theta}{r} \right) \end{cases}, \quad (\text{A15})$$

For a homogeneous isotropic medium, the constitutive relation is:

$$\sigma_{ij} = \lambda \delta_{ij} \varepsilon_{kk} + 2\mu \varepsilon_{ij}. \quad (\text{A16})$$

In the above, the projection of  $\sigma_{ij}$  in the  $z$ -direction has already been given in (A11), so we only need to compute  $\varepsilon_{rr}$ ,  $\varepsilon_{\theta\theta}$  and  $\varepsilon_{r\theta}$  from (A15). For  $r \neq 0$ , the results are:

$$\begin{aligned}
\varepsilon_{\theta\theta} &= \frac{u_r}{r} + \frac{\partial u_\theta}{r \partial \theta} \\
&= -\frac{m-1}{2r} (V_m + i W_m) J_{m-1}(kr) e^{i(m-1)\theta} \\
&\quad - \frac{m+1}{2r} (V_m - i W_m) J_{m+1}(kr) e^{i(m+1)\theta},
\end{aligned} \tag{A17.1}$$

$$\varepsilon_{rr} = (\nabla \cdot u - \varepsilon_{zz}) - \varepsilon_{\theta\theta} = -k V_m J_m(kr) e^{im\theta} - \varepsilon_{\theta\theta}, \tag{A17.2}$$

$$\begin{aligned}
\varepsilon_{r\theta} &= \frac{1}{2} \left( \frac{\partial u_\theta}{\partial r} + \frac{1}{r} \frac{\partial u_r}{\partial \theta} - \frac{u_\theta}{r} \right) \\
&= \omega_z + \left( \frac{1}{r} \frac{\partial u_r}{\partial \theta} - \frac{u_\theta}{r} \right) \\
&= \frac{1}{2} (\nabla \times u) \cdot e_z + \left( \frac{1}{r} \frac{\partial u_r}{\partial \theta} - \frac{u_\theta}{r} \right) \\
&= \frac{1}{2} k W_m J_m(kr) e^{im\theta} + \frac{i(m-1)}{2r} (V_m + i W_m) J_{m-1}(kr) e^{i(m-1)\theta} \\
&\quad - \frac{i(m+1)}{2r} (V_m - i W_m) J_{m+1}(kr) e^{i(m+1)\theta}.
\end{aligned} \tag{A17.3}$$

When  $r = 0$ , if the source depth differs from the station depth, then all displacement and strain components should converge. From the properties of  $\lim_{r \rightarrow 0} J_m(kr)$  and the recurrence relation (A7.2), we have, For  $m = 0$ :

$$\varepsilon_{\theta\theta} = \frac{k}{4} (V_0 + i W_0) e^{-i\theta} - \frac{k}{4} (V_0 - i W_0) e^{i\theta}, \tag{A18.1}$$

$$\varepsilon_{rr} = -k V_0 e^{i \cdot 0\theta} - \varepsilon_{\theta\theta}, \tag{A18.2}$$

$$\varepsilon_{r\theta} = \frac{1}{2} k W_0 e^{i \cdot 0\theta} + \frac{ik}{4} (V_0 + i W_0) e^{-i\theta} + \frac{ik}{4} (V_0 - i W_0) e^{i\theta}. \tag{A18.3}$$

For  $m = 1$ ,

$$\varepsilon_{\theta\theta} = 0, \tag{A18.4}$$

$$\varepsilon_{rr} = 0, \tag{A18.5}$$

$$\varepsilon_{r\theta} = 0. \tag{A18.6}$$

For  $m = 2$ ,

$$\varepsilon_{\theta\theta} = -\frac{k}{4} (V_2 + i W_2) e^{i\theta}, \tag{A18.7}$$

$$\varepsilon_{rr} = -\varepsilon_{\theta\theta}, \tag{A18.8}$$

$$\varepsilon_{r\theta} = \frac{ik}{4} (V_2 + i W_2) e^{i\theta}. \tag{A18.9}$$